Characterization of acoustic sources in a corrugated pipe flow with linear stochastic estimation

Gaëtan Galeron, M Amielh, Pierre-Olivier Mattei

JASA ARTICLE

Characterization of acoustic sources in a corrugated pipe flow with linear stochastic estimation

Gaëtan Galeron,[1] Muriel Amielh,[2,a)] and Pierre-Olivier Mattei[1]

[1]*Aix Marseille Université, Centre National de la Recherche Scientifique, Centrale Marseille, Laboratoire de Mécanique et d'Acoustique, Unité Mixte de Recherche 7031, Marseille, France*

[2]*Aix Marseille Université, Centre National de la Recherche Scientifique, Centrale Marseille, Institut de Recherche sur les Phénomènes Hors Equilibre, Unité Mixte de Recherche 7342, Marseille, France*

ABSTRACT:

The intense whistling of corrugated pipe under flow is related to a coherence between the dynamics of structures developing in the shear layer over cavities and acoustic eigenmodes of the pipe. In order to highlight the coupling between aerodynamics and acoustics, three measurement systems with complementary characteristics in terms of space and time resolutions are synchronized. The simultaneity of the measurements of velocity and acoustic pressure provided by five local probes, as two hot-wires and three microphones, with the velocity fields measured by PIV in the same flow region is used to estimate the velocity fields at frequencies compatible with the space-time characterization of the acoustic sources. The linear stochastic estimation (LSE) is performed to reconstruct these high frequency velocity fields. Two rectangular corrugated pipes with different corrugation geometry are investigated. Thanks to the LSE velocity field reconstruction, the contribution of the flow structures, both jet flapping and vortex shedding, to acoustic level is highlighted. © *2021 Acoustical Society of America*. https://doi.org/10.1121/10.0008897

(Received 29 July 2020; revised 18 October 2021; accepted 9 November 2021; published online 13 December 2021)

[Editor: David E. Scarborough] Pages: 4268–4282

I. INTRODUCTION

Due to their properties of overall flexibility and local rigidity, corrugated pipes are used in many fluid transport applications. Under certain conditions of geometry and flow, these pipes can whistle, thus generating vibrations harmful to the adjoining industrial installations. This intense whistling is attributed to the coherence between the structures that develop in the shear layer flush with each cavity, and the sound propagation related to the longitudinal acoustic modes of the pipe (Nakiboglu, 2012). The vortex or vortices that are established in each cavity, the turbulence of the flow, the interaction between the cavities constituting the corrugation, and finally the feedback of the whistling on the flow are related to the geometry of the pipe. The correlation between the flow and the acoustic eigenmodes of the pipe is studied here.

Nakamura and Fukamachi (1984, 1991) conducted wind tunnel measurements to study the acoustic oscillation in a corrugated tube under flow open at both ends. They conclude that the sound is emitted by coupling of the unstable shear layer with longitudinal acoustics modes of the tube, which correspond to an approximatively harmonic series of frequencies. The resulting instability is characterized by a self-excited resonant oscillation occurring in the fluid-acoustic coupled system. Nakamura and Fukamachi suggest that the acoustic oscillation in a corrugated tube is caused by swirling sound sources according to the theories of Powell (1964) and Howe (1975). Hammache *et al.* (1993) carried out experimental work similar to that of Nakamura and Fukamachi, where the study of the sound production mechanism was performed in various corrugated geometries in a wind tunnel using hot-wire probes and microphones. Their parametric study determined the minimum number of corrugations necessary for the tube to emit a sound. One of the results they reported was that in the presence of a single corrugation at the entrance of a tube, the position of the pressure node on a cavity ensures the possibility of whistling. In addition, they have shown that the pressure node is the place of generation of sound by mapping pressure and velocity, which Golliard and Tonon (2010), Tonon *et al.* (2010), Nakiboglu *et al.* (2010), and Nakiboglu and Hirschberg (2012) subsequently confirmed. They observed in particular that the increase in the depth of the corrugation lowered the fundamental frequency, just like the increase in the width of the plateau compared to the cavity opening length for cavities whose pitch Pt (periodicity of the corrugations) is the sum of a plateau length $Pt - (w + r_1 + r_2)$ and the cavity opening length $(w + r_1 + r_2)$ as sketched in Fig. 1.

Focused on the application of gas transport, the object of the study is limited to pipes of great length compared to the characteristic dimensions of the cavities. Since the first cavity is described to play a main role in the whistling triggering, the experiments conducted here aim to investigate the structuration of the flow around the first cavity for two rectangular corrugated pipe configurations with different geometry. Quantifications of the spatial organization of the

a)Electronic mail: muriel.amielh@irphe.univ-mrs.fr

https://doi.org/10.1121/10.0008897

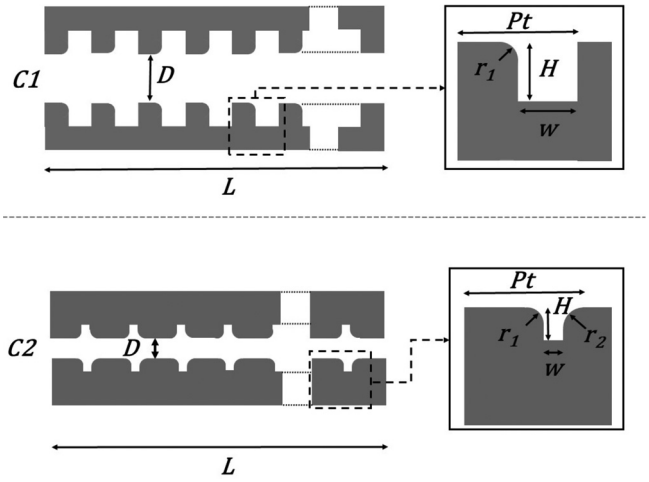

FIG. 1. Internal geometry of the two studied configurations of corrugated pipes (top view).

flow around corrugations related to the flow induced acoustics, other than by one-point velocity measurements by hot wire associated with acoustic measurements by microphone, are scarce and difficult to carry out in a corrugated tube of circular geometry. The works describing the velocity field and the vorticity are mainly based on numerical simulations (Popescu *et al.*, 2011; Nakiboglu *et al.*, 2011).The implementation of optical diagnostics such as PIV in this type of geometry is difficult because of optical distortions. Geveci *et al.* (2003) have solved this problem by machining local very thin wall in their study on a axisymmetric shallow single cavity with sharp edges ($L/H = 5$) and develop analyzes based on phase-averaged velocity fields. To avoid the optical distortions, the present experiment consists in the study of the acoustic resonance in a corrugated tube in a geometry of rectangular cross section, almost 2D plane, since the ratio of the transverse span B over the vein core dimension D is $B/D \geq 5$. The investigated flow velocity range corresponds to Mach number lower than 0.1. The experimental set-up developed to study whistling corrugated pipes is described in Sec. II. The geometry of the pipe is given together with the complementary three devices, which consist in low space/high temporal resolution probes (two hot-wires and three microphones) and a high spatial/low temporal resolution system (particle image velocimetry), used for velocity and acoustic pressure measurements. Section III is dedicated to the description of the flow. Section IV is devoted to the identification of the acoustic modes by their associated frequencies and sound pressure levels according to flow conditions and pipe geometry. The simultaneity of the measurements provided by the five probes with the particle image velocimetry (PIV) fields is used to implement a linear stochastic estimation (LSE) which principle is recalled in Sec. V. This method initially proposed by Adrian (1979) and developed by Adrian and Moin (1988) is mainly used to detect coherent structure in turbulent flows (Pey *et al.*, 2012; Piponniau *et al.*, 2014; Graziani *et al.*, 2015) and gives a reconstruction method to obtain high space-time resolved velocity fields. Associated to proper orthogonal decomposition (POD), the dynamics of most energetic structures in turbulent flows can be described quantitatively. While the study of Durgesh and Naughton (2010) improves the combination LSE-POD by testing multi-time delay, the extension of LSE in the spectral domain by Tinney *et al.* (2006) has open new development to improve the POD efficiency giving a reconstruction of POD modes from non time resolved PIV quite comparable to those obtained from time resolved PIV as demonstrated by Zhang *et al.* (2020).

In the present study, results from direct LSE reconstruction in the space-time domain allow the identification and quantification of the dynamics of the flow with details that cannot be achieved by current available optical diagnostics alone, but only with high-speed PIV as used by Koschatzky *et al.* (2011a) and Koschatzky *et al.* (2011b) in their study of a flow around a shallow single cavity with sharp edges ($L/H = 2$). From the analyses of LSE results developed in Sec. VI, the aeroacoustic sources are found to be vortices developing in the shear layer located between the vena contracta and the cavity aperture. The contribution of this vortices to acoustic power is also analysed in this section. Section VII concludes the paper.

II. EXPERIMENTAL SET-UP

A. Corrugated pipe

Experiments are performed successively for two types of corrugated pipes C1 and C2 presented in Fig. 1. Each corrugated pipe is connected to a blower with a motor fan (Fig. 2) that provides a velocity of up to $30\,\mathrm{m\,s^{-1}}$ (Amielh *et al.*, 2014). The cross section of the corrugated pipe is rectangular to facilitate optical access, with a span $B = 100\,\mathrm{mm}$ and a vein core of transversal dimension D. Each pipe is laterally corrugated along its length L through N cavities placed opposite. The upper and lower walls are smooth. Each cavity is characterized by its depth H and its bottom width w (Fig. 1). The upstream edge of each cavity is rounded with a radius of curvature r_1. For the first geometry C1, totally machined in Plexiglas of 20 mm thickness, the downstream edge of the cavity is sharp. The cavities of the second geometry C2 were designed to be similar to an

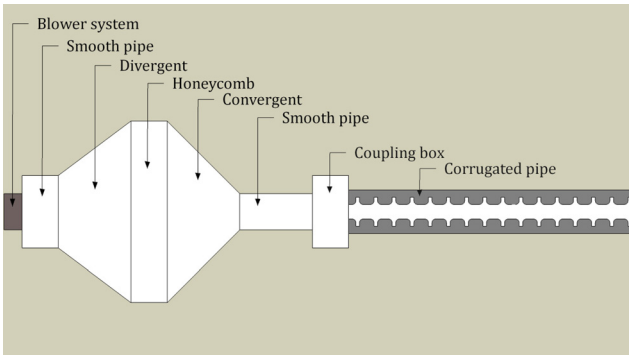

FIG. 2. (Color online) Sketchup of the experimental setup.

industrial riser with narrow cavities and upstream and downstream rounded edges. Lateral corrugated plates were machined in aluminium of 20 mm thickness for C2 while the top and bottom plates, in Plexiglas, are the same as for C1. The downstream radius of curvature is r_2. Each geometry generates a pattern whose pitch is Pt. The dimensions of each configuration C1 and C2 are given in Table I. The length L and the vein core dimension D were adapted for each configuration in order to obtain a strong whistling for the available flow rate range generated by the blower.

The specificity of the present experiments is the rectangular cross section of the channel where the potential effects of corner flow are questionable. However, the corners between the smooth (top or bottom) plate and a lateral corrugated plate are clearly geometrical configurations extremely complex and far from the main studies on secondary corner flows in rectangular smooth duct. The simulations of Vinuesa *et al.* (2014) for a rectangular smooth duct with the same aspect ratio ($AR = 5$) than for our configuration C1 show that 40% of the central area is not influenced by corner vortices. In terms of aspect ratio, the configuration C2 ($AR = 12.8$) is closer to the more recent simulations of Vinuesa *et al.* (2018), where secondary flows in an $AR = 10$ rectangular smooth duct were investigated. These simulations show that 75% of the central area is not influenced by corner vortices for $AR = 10$. The recent numerical study of Mahmoodi-Jezeh and Wang (2020) presents some results for a square duct with only the bottom plate covered with rib elements, while the three other plates are smooth. One of their parameters is the blockage ratio, Br, that is the ratio of height of rib over height of channel. The maximal Br for their study is $Br = H/(D + H) = 0.2$ and the Reynolds number is $Re = 5600$. We calculate $Br = 2H/(D + 2H) = 0.5$ ($Re \approx 29\,000$) for our configuration C1 and $Br = 2H/(D + 2H) = 0.59$ ($Re \approx 12\,000$) for C2. These simulations show a significate mean streamwise vorticity in the bottom corner where the ribbed plate and the lateral smooth plate join up, but no center of vortex is identified in this region. Longitudinal vortices are only detected in the corner of two smooth plates. Moreover, these authors indicate that the magnitude of mean streamwise vorticity decreases near this bottom corner of the duct as the blockage ratio increases. So, the junction of a ribbed (corrugated) plate with a smooth plate in a channel with a high blockage ratio Br as in our configurations is not favorable for the corner vortex development.

With an aspect ratio $AR = B/D = 5$ for C1, respectively, $AR = 12.8$ for C2, these configurations can be considered two-dimensional and so present similarities with the pipes with multiple side cavities studied by Tonon *et al.* (2010).

Whereas configurations C1 and C2 have the distinction of having a ratio $D/2H \leq 1$ which is a configuration hitherto unexplored in the literature to our knowledge if we only considered this geometric parameter, the equivalent ratio of the channel volume to the cavity volume is estimated to $DPt/2Hw = 2$ for C1 and 4 for C2 in quasi two-dimensional geometry. Thus, the present experiments remain in the range of experiments of Nakiboglu (2012) in circular corrugated pipe in terms of this volume ratio.

The inlet of the pipe is connected to the blower by using a rectangular coupling box of large cross section with the dimensions $170 \times 350 \times 350\,\text{mm}^3$ which, by simulating an open end, notably ensures a pressure node at the inlet of the corrugated pipe. It also ensures airtightness at the connection between the blower and the pipe. The corrugated pipe is open downstream to also provide a pressure node. The Cartesian coordinate systems (O, X, Y) associated with each configuration are presented in Fig. 3 where the positive X-direction is that of the main flow.

B. Velocity measurements by PIV

For the investigation of the flow around the first cavity in the configurations C1 and C2 (Fig. 3), velocity field measurements by PIV are performed by illuminating the flow with a laser sheet positioned horizontally at mid-height of the span (at B/2). The laser is a high energy pulsed Nd: YAG (200 mJ) at 10 Hz (QuantaRays, Spectra-Physics) and 532 nm wavelength. The tracer used is a micron aerosol of olive oil injected upstream of the coupling box. Images were acquired with a Kodak ES 1.0 camera (1008×1018 pixels) for experiments in the C1 configuration and with a FlowSense EO 4 M-32 camera (2072×2072 pixels) in the C2 configuration. 950 pairs of images are acquired at a rate of 10 Hz for each experiment. Post-processing is performed

TABLE I. Dimensions of the two studied configurations of corrugated pipes C1 and C2.

Dimension	C1	C2
L	2 m	1 m
D	20 mm	7.8 mm
Pt	20 mm	20 mm
H	10 mm	5.6 mm
w	10 mm	3.4 mm
r_1	3 mm	2.8 mm
r_2	0 mm (sharp)	3.5 mm
N	100	50
H/w	1	1.6

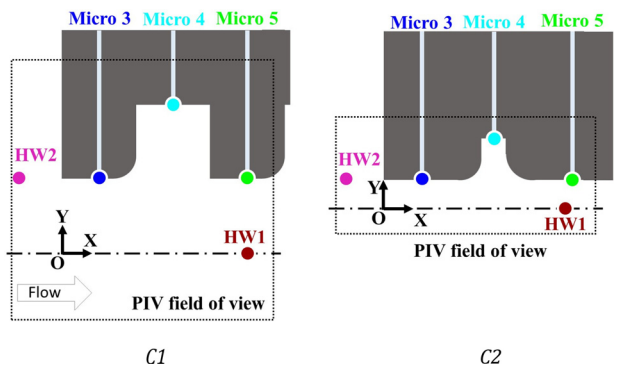

FIG. 3. (Color online) PIV field of view and positioning of the 5 sensors: 2 hot-wires (HW1 and HW2) and 3 microphones (Micro 3, 4, 5) around the first cavity for the two configurations C1 and C2.

https://doi.org/10.1121/10.0008897

with DYNAMICSTUDIO software (DANTEC Dynamics) using the "adaptive correlation" function on boxes of 32×32 pixels for C1 and 16×16 pixels for C2, both with 50% overlap. A velocity vector is thus calculated on each box of $0.59 \times 0.59\,\text{mm}^2$ in the field of view of $36 \times 36\,\text{mm}^2$ for C1 and on boxes of $0.19 \times 0.19\,\text{mm}^2$ in the field of view of $31 \times 31\,\text{mm}^2$ for C2. Only one cavity on one side of the symmetry axis is explored, because on the opposite side a slot of 3 mm plugged with a glass window was arranged at mid-height of the span (at B/2) to let laser sheet illuminate inside the pipe. The wall where laser sheet impacts was painted with a fluorescent paint in order to limit light reflection in the 532 nm wavelength. During experiments, each camera was equipped with a narrow passband filter at 532 nm.

C. Velocity measurements by hot-wire

For both configurations C1 and C2, the hot-wire velocity measurements are made at two points at mid-height of the span (at B/2). The HW1 hot-wire is a 55P11 (DANTEC Dynamics) type probe with straight prongs. The HW2 hot-wire is a 55P05 (DANTEC Dynamics) type probe with offset prongs, dedicated to boundary layer measurements. This probe makes it possible to approach the wall at the entrance of the vein. It is positioned at ($X = -5$ mm, $Y = 10$ mm). Previous measurements (Amielh *et al.*, 2014) have shown that in this position, the probe is located on a maximum of acoustic particle velocity that corresponds to a minimum of acoustic pressure related to Dirichlet condition in pressure at the inlet thanks to the coupling box. Thus, acoustic particle velocity is effectively captured by the hot-wire HW2. Moreover, for the experimental set-up of the configuration C1, the laser sheet intercepts the sensitive part (diameter 5 μm, length 1.25 mm) of this hot-wire with each flash. This causes a destabilization of the velocity signal, which will be shown later (see Sec. VI A), over two acquisition time steps ($2 \times 1/25\,600 = 78\,\mu$s). This event is intentionally used to synchronize the PIV and the sensor signals for PIV measurement in C1 configuration. When the flow conditions in the corrugated pipe stimulate the whistling, the velocity signal sensed by the hot-wire HW2 is sinusoidal in time. This property is used to correct the velocity signal disturbed by the laser flash. For the experimental set-up of the C2 configuration, the synchronisation was insured by registering simultaneously the probes signals and the timer box signal that controls laser flashes and camera acquisition. For the flow characterisation, the hot-wire HW1 is positioned 20 mm upstream from the downstream pipe outlet on the symmetry axis. The mean velocity measured at this position is retained as the reference velocity U_0 used hereafter. Measurements at this position aims to measure the turbulence level developed all along the pipe. For the LSE method application, the hot-wire HW1 is placed at ($X = 25$ mm and $Y = 0$ mm) downstream of the channel inlet.

D. Acoustics pressure measurements by microphone

The acoustic pressure measurements are carried out on the wall with three GRAS 40SC microphones, type IEPE, each equipped with a 320 mm silicone extension tube allowing the body of the sensors to be placed outside the flow. The microphones (Micro 3, 4, and 5) were previously recalibrated in a Kundt tube to take into account the influence of these tube extensions on the sensitivity of the sensors. The flush pressure taps are located at the following positions: Micro 3 on the first plateau, Micro 4 at the bottom of the first cavity, and Micro 5 on the second plateau. The exact locations of the five probes are given in Table II in the coordinate system of each corrugated pipe.

E. Acquisition of five probe signals

The acquisition of the sensor signals is carried out simultaneously on a National Instruments acquisition unit at a sampling frequency F_s equal to 25 600 Hz (Chassis NI cDAQ-9188). The two hot-wires are connected to a NI 9215 (16-bit) module, while the three IEPE-type microphones are connected to an NI 9234 module that provides both the power supply and the 24-bit acoustic signal. For the experiments in the C2 configuration, the timer box signal is also acquired on the A/D card NI 9215 in order to synchronise the PIV images and the probe signals. A program (Virtual Instruments) designed under LABVIEW is piloting this acquisition. Post-treatments are done with MATLAB. To cover the acquisition time at 10 Hz of 950 PIV fields, the acquisitions of the sensor signals last $Ts = 100$ s; 2 560 000 samples are acquired per channel of the A/D cards.

III. DESCRIPTION OF THE FLOW

Measurements of the velocity fields by PIV furnished information on the spatial organisation of the flow. By considering the Reynolds decomposition, each instantaneous velocity component $V(t)$ is constituted of a mean component $\bar{V}$ and a fluctuating component $V'(t)$ with $\overline{V'} = 0$. We write for the streamwise component along x and the transverse component along y, respectively,

$$\begin{aligned} u(x,y,t) &= \bar{u}(x,y) + u'(x,y,t), \\ v(x,y,t) &= \bar{v}(x,y) + v'(x,y,t). \end{aligned} \tag{1}$$

For the C1 configuration, the flow around the first cavity is investigated using PIV measurements for several flow rate conditions corresponding to U_0 in the range 10–25 m s^{-1} associated with a Mach number $M = U_0/c_0$ in the range 0.02 to 0.08 with the speed of sound $c_0 = 343$ m s^{-1} at

TABLE II. Positions of the five probes for the two studied configurations of corrugated pipes C1 and C2.

	Probe positions (X,Y) in mm	
Probes	C1	C2
HW1	(25, 0)	(25, 0)
HW2	(−5, 10)	(−5, 3.9)
Micro3	(5, 10)	(5, 3.9)
Micro4	(15, 20)	(14.8, 9.5)
Micro5	(25, 10)	(25.2, 3.9)

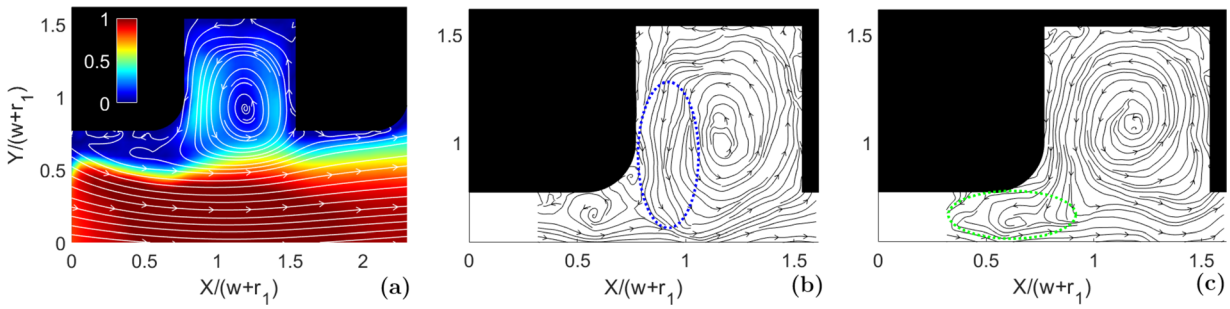

FIG. 4. (Color online) Velocity fields measured by PIV in a zoomed area just around the cavity 1 for M = 0.054, for the C1 configuration. (a) Mean velocity magnitude $\sqrt{\bar{u}^2+\bar{v}^2}/U_0$ and mean streamlines, vena contracta in dark red. (b), (c) Snapshots of streamlines: fluid ejected by the vortex is re-entrained by the main flow (blue region) or supplies the upstream recirculating region (green region).

ambient conditions. As shown for C1 in Fig. 4(a) for $M = 0.054$, the main flow is accelerated at the entry by a vena contracta. One counterclockwise vortex sits inside the cavity. A part of the flow ejected from the cavity supplies a recirculating region between the upstream round edge of the cavity and the edge of the vena contracta. The other part is re-entrained by the central main flow. This behaviour is specific to the first cavity. However, this formal representation of the mean flow obtained from the statistics calculated over the 950 PIV fields is misleading for the interpretation because the position of the vortex center fluctuates according to the flapping of the edge of the vena contracta. As shown by a snapshot in Fig. 4(b) associated with a whistling at 600 Hz (mode 8) the recirculation zone is sometimes supplied by flow ejected by the vortex while later all the fluid ejected from the cavity is re-injected in the main flow, see Fig. 4(c). All these regions are guessed to play a role in the resonance, but PIV measurements alone acquired at 10 Hz do not give information on temporal scenario. For flow condition where no resonating mode is detected ($U_0 < 10\,\mathrm{m\,s^{-1}}$), the flow organisation is observed from PIV fields to be almost the same with the presence of a vortex inside the cavity. However, in the presence of strong whistling, the shear layer located between the main flow and the cavity aperture shows larger transversal oscillations that is confirms by larger turbulence level in this region.

For the C2 configuration, the flow investigation by PIV was focused on two particular conditions. The first one corresponds to a 0.037 M number with no acoustic oscillation detected, while the second condition for $M = 0.069$ is associated with a strong whistling at 1231 Hz (mode 8). When no resonating mode is installed, the flow is sufficiently stable so that two vortices take place inside the cavity thanks to a ratio H/w larger than 1. This is observed on PIV field snapshots and clearly in the mean flow representation shown in Fig. 5(a). In this situation, the vortex located at the aperture of the cavity keeps the shear layer away from any interaction with the wall. For the studied condition with whistling, only one vortex is observed inside the cavity both on the mean flow [Fig. 5(b)] and on any PIV field snapshot [Fig. 5(c)]. The shear layer between the vortex edge and the main flow gets closer to the cavity aperture. Note that in the areas very close to the walls, PIV measurements were particularly difficult because of the laser reflections on the walls despite the care taken to treat this problem.

In order to statistically characterize this interface region between the cavity 1 and the flow on the axis of the channel, we consider the contribution of fluctuations of components u and v to turbulent kinetic energy. We thus present in Fig. 6 the evolution of the region where the quantity $k = \frac{1}{2}(\overline{u'^2} + \overline{v'^2})$ is high, as a function of Mach number. This region coincides with the sheared layer. In the absence of strong whistling (case $M = 0.029$), the region where k is maximal ($k = k_{\max}$) remains localized outside cavity, this observation is common for both configurations C1 and C2 [Figs. 6(a) and 6(c)]. When the whistling is intense, the zone of large values of k enlarges transversally for the C1 configuration [Fig. 6(b)], while this lateral extension is not so clear for the C2 configuration. In this latter case, the specificity is an incursion of the shear layer in the cavity aperture [Fig. 6(d)]. In these both cases of strong whistling, statistically, some flow characterized by $k = k_{\max}$ hits the downstream edge of the cavity.

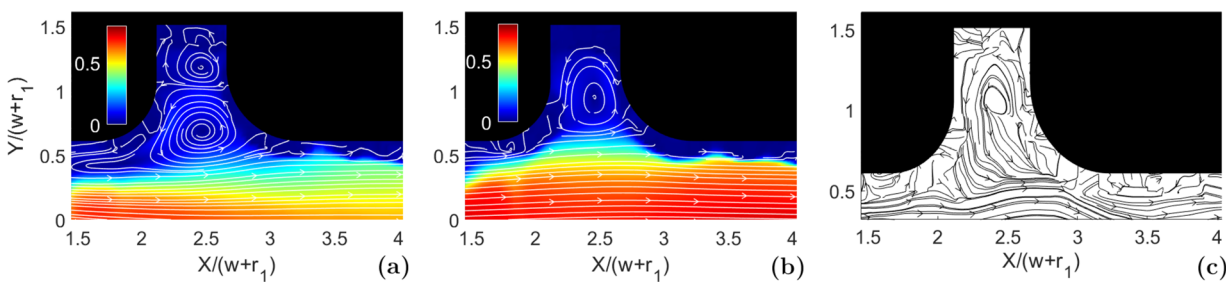

FIG. 5. (Color online) Velocity fields measured by PIV in a zoomed area just around the cavity 1 for C2 configuration. Mean velocity magnitude $\sqrt{\bar{u}^2+\bar{v}^2}/U_0$ and mean streamlines (a) for M = 0.037, (b) for M = 0.069. (c) Snapshots of streamlines for M = 0.069.

https://doi.org/10.1121/10.0008897

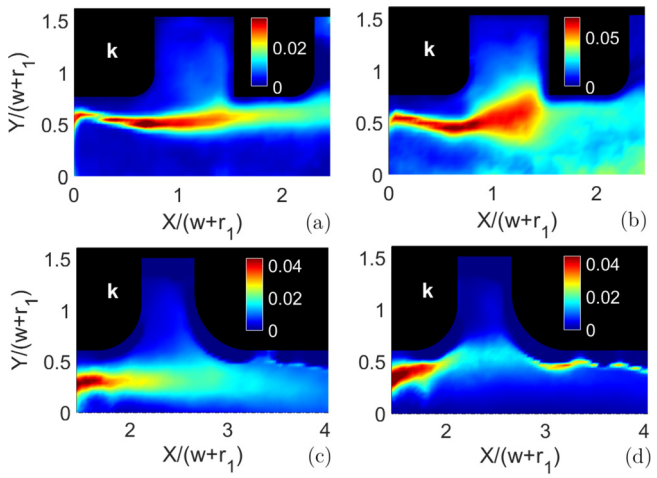

FIG. 6. (Color online) Contribution to the kinetic energy $k = \frac{1}{2}(\overline{u'^2} + \overline{v'^2})/U_0^2$ with no whistling (left) and strong whistling (right) for M = 0.029 (a) and M = 0.054 (b) for the C1 configuration and for M = 0.037 (c) and M = 0.069 (d) for the C2 configuration.

IV. CHARACTERIZATION OF THE ACOUSTIC MODES OF THE CORRUGATED PIPES UNDER FLOW

A series of measurements consisted in characterizing the aeroacoustics of the corrugated pipes by increasing the velocity U_0 of the flow between 10 and 25 m s^{-1}. It was determined that the presence of the corrugations modifies the effective speed of sound c_{eff}, which must be taken into account to predict the acoustic longitudinal eigen modes. For the C1 configuration, the frequencies f_n of the n longitudinal modes of this pipe were estimated by the relation $f_n = nc_{eff}/2L_{eff}$ with $c_{eff} = 299$ m s^{-1}, with $L_{eff} = L + 2\delta L = 2.02$ m, the length of the pipe including the acoustic length correction at the extremities. These effective parameters were experimentally determined by previous measurements (Amielh *et al.*, 2014). For the C2 configuration, the acoustic length correction was not determined experimentally, but was supposed to vary with the D dimension by analogy with a circular duct. By considering that δL is equal to 10 mm for C1 configuration with $D = 20$ mm, we estimate $\delta L = 3.9$ mm for the C2 configuration with $D = 7.8$ mm. According to the frequencies of the different modes observed when the C2 pipe is under flow, the effective speed of sound is found to be $c_{eff} = 317$ m s^{-1}. The fundamental mode for C2 is at 157 Hz.

The velocity signals were measured by the hot-wire HW2 positioned as described in Fig. 3 and the hot-wire HW1 at 20 mm before the downstream end of the corrugated pipe at exactly $X = 1981$ mm for C1 and $X = 980$ mm for C2, and $Y = 0$ mm. Details of spectral analyses are given for the C1 configuration. For U_0 less than 10 m s^{-1} ($M < 0.03$), spectral peaks for mode 3 as predominant mode and modes 4 and 5 as secondary modes emerge in the spectral analyses of the microphones signals, but with sound pressure level lower than 70 dB. Modes 1 (at 75 Hz) and 2 are not identifiable with our analyses. It is usual not to observe the first longitudinal eigenmode in corrugated pipe due to thermoviscous losses as stipulated in the whole bibliography of corrugated pipes. A large increase in sound pressure level (measured with microphone Micro 4 in configuration C1) occurs for velocities above $U_0 = 12$ m s^{-1} ($M = 0.035$) associated with the emergence of the fifth mode as corroborated by Figs. 7(a) and 8(c). The power spectral density of velocity measured by the downstream hot-wire [Fig. 7(b)] shows that the hot-wire is sensitive to the acoustics velocity and moreover that this great amplification is concomitant with an emergence of the amplitude of energy associated with the preferred mode from the spectral turbulence level. For both configurations, Fig. 8(a) presents the evolution of the Helmholtz number $He = f_n L_{eff}/c_{eff}$ versus the Mach number M. In the studied flow conditions, the main modes are observed up to the ninth mode. These modes are associated with a Strouhal number $Sr = f_n(w + r)/U_0$ which varies between 0.30 and 0.40 [Fig. 8(b)] in agreement with the results of the literature on "singing risers" (Nakiboglu *et al.*, 2010). For C1 pipe, the whistling becomes intense (>100 dB) when the velocity at the pipe outlet, U_0, exceeds 12 m s^{-1} [$M > 0.03$, see Fig. 8(b)] reaching a sound pressure level of 120 dB at 25 m s^{-1}. This is accompanied by a marked increase in the velocity standard deviation U_{rms} in the upstream part of the corrugated pipe [Fig. 8(d)]. In this region, the flow is not turbulent and the hot-wire is highly sensitive to the acoustic particle velocity, so that the trace of the modes is perceived as on the acoustic pressure signal. On the other hand, when the hot-wire HW1 is placed at the downstream end of the pipe C1 ($X = 1981$ mm), the turbulence has developed all along the pipe and the standard deviation increases linearly according to the U_0 velocity, masking thus the acoustic effect. For the C2 configuration, the dip observed for the sound pressure level evolution around M = 0.06 in Fig. 8(c), and also for U_{rms} in Fig. 8(d), between the modes 6 and 7 is probably not only due to a sharing of the energy between

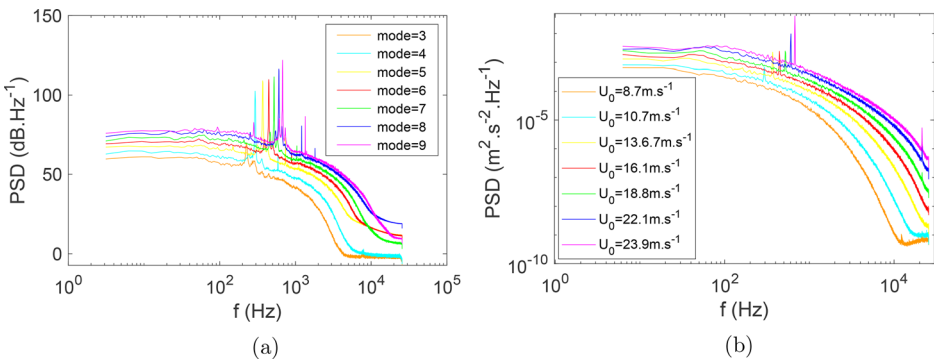

FIG. 7. (Color online) Spectral analysis for C1 configuration: (a) from acoustic sound pressure level measured inside the cavity 1 (Micro 4, decibel reference 2×10^{-5} Pa), (b) from velocity measured by the downstream hot-wire (HW1 at X = 1981 mm). Sampling frequency Fs = 51200 Hz.

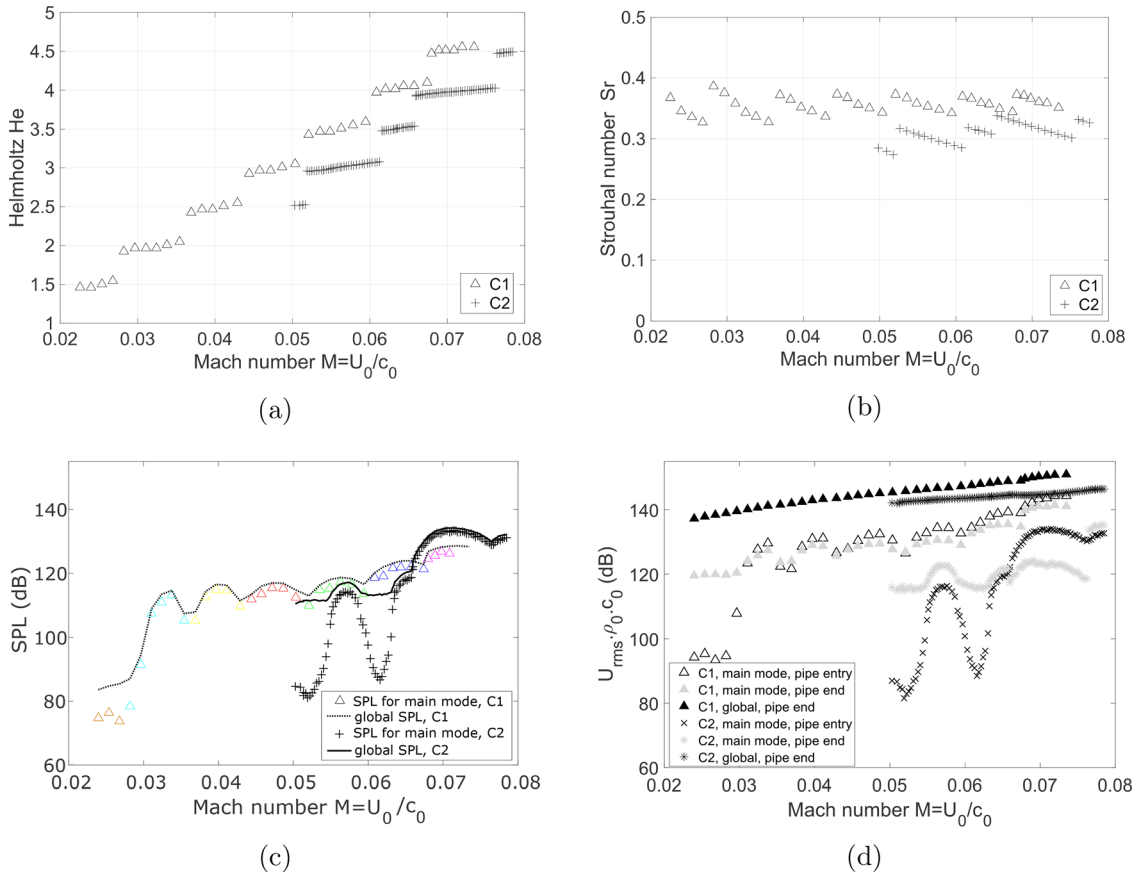

FIG. 8. (Color online) Characterisation of acoustic modes of the corrugated pipe with flow for C1 and C2 configurations: (a) Helmholtz number associated with the frequency of the main mode, (b) Strouhal number associated with the main mode, (c) acoustic sound pressure level (decibel reference 2×10^{-5} Pa), (d) velocity root mean square measured by hot-wires.

these two pipe modes, since the mode 6 and 7 frequencies of the corrugated pipe C2 might be in interference with longitudinal resonance modes of the rectangular coupling box (see Sec. II A) ranging between 1000 and 1100 Hz according boundary conditions on the coupling box faces. This frequency range is obtained when considering for pressure Neumann boundary conditions on lateral faces, Dirichlet boundary conditions on flow exit face and Neumann or Dirichlet ones for the flow entry face, since the suitable boundary condition is probably an intermediate one between both. The global acoustic level is also plotted in Fig. 8(c) showing that, except when two successive modes are concurrent or concomitant with coupling box modes, the whole acoustic level is contained in the main mode.

V. LSE METHOD

The LSE method implemented makes it possible to reconstruct velocity fields resolved spatio-temporally from two types of measurement. A measuring device is resolved spatially, in our case PIV, and probes signals are resolved temporally, in our case microphone and hot-wire signals (Pey *et al.*, 2012; Piponniau *et al.*, 2014; Graziani *et al.*, 2015). The reconstruction method is then based on a mathematical development detailed below. For the present measurements, there are PIV fields resolved spatially, but of low temporal resolution (sampling frequency of 10 Hz): $\{u'(x_{pq}, t_i)\}_{(i=1,\ldots,m)}$ with m the number of PIV fields (here $m = 950$) and $p \times q$ the number of positions in the PIV field (here 53×34 and 84×63 in the regions of interest for C1 and C2, respectively). The simplified notation x_{pq} indicates that the position considered in the PIV field are taken at the coordinates $(X_{P=1,\ldots,p}, Y_{Q=1,\ldots,q})$. The probes of high temporal resolutions (sampling frequency of 25 600 Hz), but punctual (lack of spatial resolution) take the values: $\{s'(j,t)\}_{(j=1,\ldots,n)}$ (with n the number of probes, here $n = 5$). The five probes are respectively HW1, HW2, Micro 3, Micro 4, and Micro 5 located at the positions specified in Table II.

In practice, fluctuating signals normalized by standard deviation are used. From these two types of measurements, the LSE method can be applied to stochastically reconstruct the velocity fields with much better temporal resolution. It is then possible to know the velocity with a very good spatiotemporal resolution. For this, the matrices A and B_{m_j} are used, where it is convenient to define m as either x or y. Their coefficients are, respectively, deduced from the cross-correlations between the probes and from the cross-correlations between the probes signals s' and PIV fields u' (and v' respectively),

https://doi.org/10.1121/10.0008897

$$\begin{cases} A_{ij} = \overline{s'(j,t)\, s'(i,t)} \\ B_{x_j}(x_{pq}) = \overline{u'(x_{pq},t_i)\, s'(j,t_i)} \\ B_{y_j}(x_{pq}) = \overline{v'(x_{pq},t_i)\, s'(j,t_i)} \end{cases}. \quad (2)$$

From each pair of matrices A and B_{m_j} we deduce the matrix Λ_{m_j} which verifies the equation $A\Lambda_{m_j} = B_{m_j}$. The latter defines the stochastic coefficients $\lambda_{m_j}(x_{pq})$. From these coefficients, a linear estimate of the fluctuating velocity field $\widetilde{u'}$ (and $\widetilde{v'}$, respectively) is proposed,

$$\widetilde{u'}(x_{pq},t) = \sum_{j=1}^{n} \lambda_{x_j}(x_{pq})\, s'(j,t). \quad (3)$$

Reconstructed instantaneous velocity fields are then deduced multiplying $\widetilde{u'}$ (and $\widetilde{v'}$, respectively) by standard deviation and adding mean velocity.

VI. RESULTS

A. Probe signals and PIV fields

The LSE method was applied for one strong whistling flow condition for each configuration C1 and C2. The common parameter of these experiments is a same instruction given to the blower motor rotation. As the head losses and cross-sections are different for the two pipe configurations, flow conditions in terms of reference velocity U_0 are different, but the resonating mode is the eighth mode for both chosen flow conditions at the frequencies $f_{wh} = 600$ and 1231 Hz, respectively, for C1 and C2. These selected conditions correspond to $U_0 = 21.7\,\mathrm{m\,s^{-1}}$ ($M = 0.063$) for C1 and at $U_0 = 23.7\,\mathrm{m\,s^{-1}}$ ($M = 0.069$) for C2.

For the selected flow condition for C1, Fig. 9(a) shows the temporal evolution of the velocity measured by the hot-wires and the pressure measured by the microphones around a laser flash associated with the measurement of an instantaneous PIV field [Fig. 9(b)]. The oscillatory nature of the microphone signals is indicative of intense whistling at the frequency of about 600 Hz (mode 8). The hot-wire signals are also sensitive to acoustics: the signal HW2 captures the acoustic particle velocity, while the turbulence of the flow is, in addition, captured by HW1 which is located inside the vein. The instantaneous PIV field shown in Fig. 9(b) illustrates the behavior of the flow around the first inlet cavity. Similar 950 snapshots acquired at 10 Hz are used to apply the LSE method.

B. LSE coefficients

The coefficients of the correlation matrix A between the probe signals [Figs. 10(a) and 11(a)] are calculated over all the measurement points using formula given in Eq. (2). Likewise, the coefficients of the correlation matrix B_{m_j} between the probes and the points of the PIV field are calculated. For this, it was necessary to perform a temporal extraction of the values of the probes at the instants of the PIV field snapshots. Actually, there are two matrices, B_{x_j} and B_{y_j}, corresponding to the velocity components (u, v) of the PIV fields in correlation with each j probe. Some illustrations of the coefficients B_{x_j} and B_{y_j} are given in Figs. 10 and 11. We can see strong correlations greater than 0.5 in absolute value between the probe signals and certain regions of the PIV field, such significative correlations enable the application of the LSE. Figure 10(e) presents the cross-spectrum between the signal of HW1 [respectively, HW2 in Fig. 10(f)] and the signal of each microphone, non-dimensionalized by-product of standard deviations of each considered signal. These results highlight that the correlation between flow and acoustics is maximal at the whistling frequency for the configuration C1, but also for the configuration C2 [Figs. 11(e), 11(f)].

C. Reconstitution of the "high frequency" velocity field by the LSE method

The determination of the matrices A, B_{x_j}, and B_{y_j} allow us to calculate the matrices Λ_{x_j} and Λ_{y_j}. Their coefficients are used [Eq. (3)] to reconstruct velocity fields at

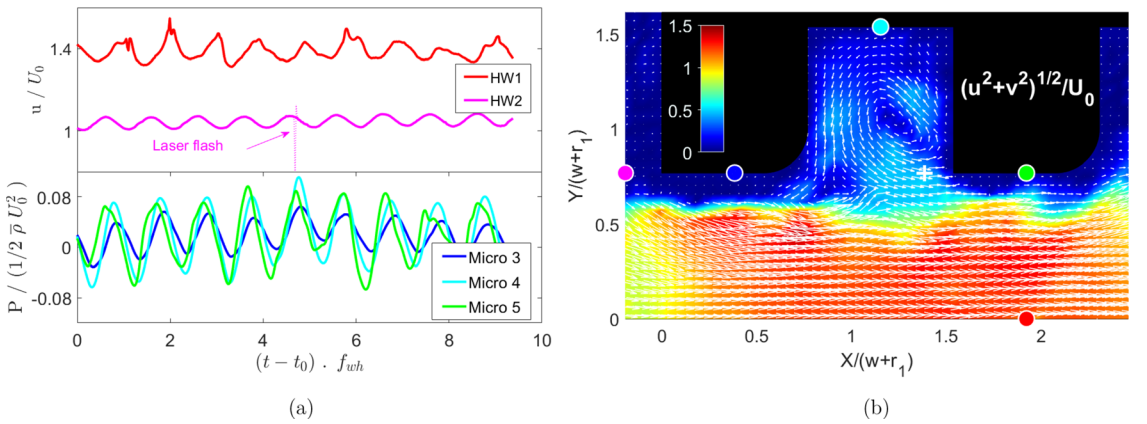

FIG. 9. (Color online) example of measurements used for LSE method for the C1 configuration. (a) Probe signals around a laser flash associated with a PIV velocity field acquisition, (b) PIV field snapshot acquired at the laser flash instant. Colored cartography: instantaneous velocity magnitude $(u^2+v^2)^{1/2}/U_0$; vectors: instantaneous $(u/U_0,\ v/U_0)$ velocity components; colored circles: location of probes, see also Fig. 3; white cross: position where an example of the LSE reconstitution of $\widetilde{u}/U_0$ and $\widetilde{v}/U_0$ is presented in Fig. 12.

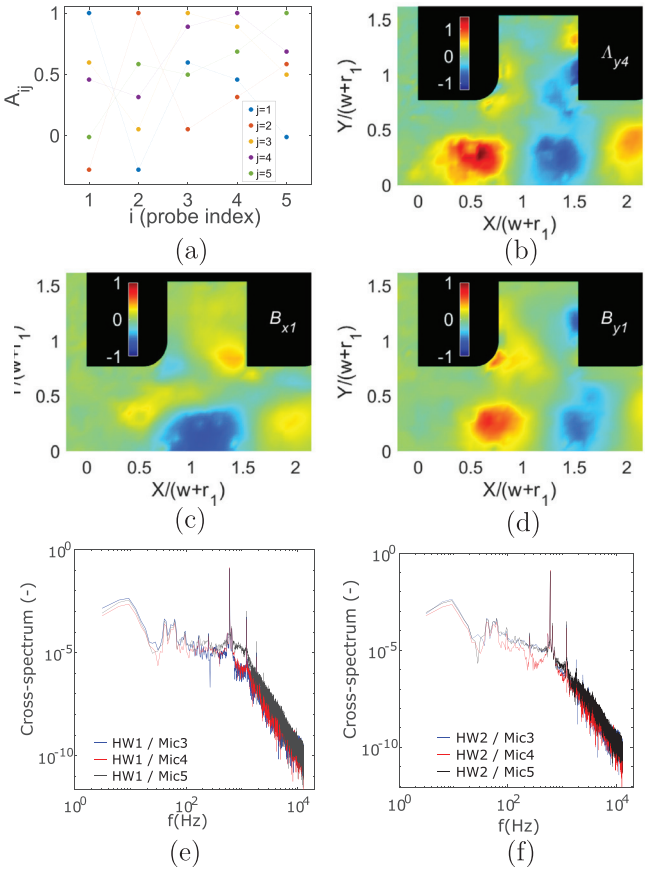

FIG. 10. (Color online) Coefficients for the LSE application to the C1 configuration: (a) Coefficients of the correlation matrix A between probe signals, (b) Λ_{y4} coefficients of the matrix Λ_{mj} for the signal of probe 4 (Micro4) and the transversal velocity component v from PIV fields, (c) B_{x1} correlation coefficients between the signal of probe 1 (HW1) and the longitudinal velocity component u from PIV fields, (d) B_{y1} correlation coefficients between the signal of probe 1 (HW1) and the transversal velocity component v from PIV fields, (e) cross-spectrum between the signal of HW1 and the signal of each microphone, non-dimensionalized by-product of standard deviations of each considered signal, (f) same caption as (e) for the signal of HW2.

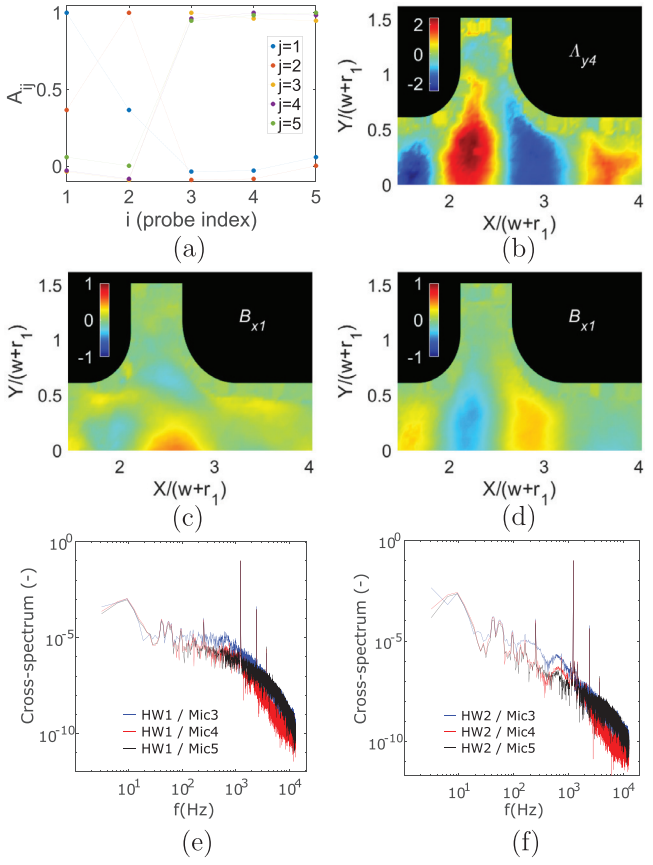

FIG. 11. (Color online) Coefficients for the LSE application to the C2 configuration. For contents of (a)–(f) see caption of Fig. 10.

intermediate times between two instantaneous PIV fields. Figures 10(b) and 11(b) present examples of the cartography of the coefficients Λ_{y_4} used for the LSE reconstruction of the velocity $\widetilde{v}$ on the observed field, respectively, for C1 and C2 configurations. Figure 12(a) gives an example of reconstruction of the time series of the components $\widetilde{u}$ and $\widetilde{v}$ velocity at the position x_{pq} corresponding to ($X = 18$ mm, $Y = 10$ mm) located near the downstream, sharp angle of the cavity for the C1 configuration. In this region, an oscillation at 600 Hz of the components u and v of velocity is highlighted.

The LSE method makes it possible to reconstruct the space-time evolution of the velocity field at the 25 600 Hz sampling frequency of the probes signals in the whole domain initially explored by PIV. An estimation of the uncertainty on the reconstructed LSE velocity field according to the number of events used for the calculations is made for the C1 configuration. One uses the coefficients of final matrix A_{ij} calculated with all available samples of probes (2 560 000 samples). One estimates correlation coefficients $B_{xj}(nb)$ and $B_{yj}(nb)$ ($j = 1, 2,\ldots5$, the index of considered probe) using nb samples (nb is varied step by step of ten samples up to the maximal $nb = 950$). The coefficients $\Lambda_{xj}(nb)$ and $\Lambda_{yj}(nb)$ are then deduced and used in order to calculate the LSE velocity fields ($\widetilde{u}(x, y, t, nb)$ and $\widetilde{v}(x, y, t, nb)$). Figure 12(b) shows how the calculation of an instantaneous LSE velocity field converges according to the number of events used in four chosen locations indicated in Fig. 12(c). This analysis is here illustrated at time t_2 (from Figs. 13 and 15) for which a maximum of amplitude of the Micro5 signal is reached. Beyond 600 events, the calculation of the instantaneous LSE velocity field is stabilized. The standard deviation of fluctuations in percentage of the local mean reference LSE velocity magnitude calculated in the range 700 to 950 events is presented in Fig. 12(c). Except near the wall upstream the cavity, where PIV was difficult to performed due to laser reflection, the LSE reconstruction is given with an error lower than 5% in a large part of the field of view.

The dynamics of the flow at different phases of the whistling period can thus be specified in the Fig. 13 which illustrates from left to right the flow cycle by snapshots of streamlines picked up at successive times t_1 to t_6 for the C1 configuration and, similarly, at t'_1 to t'_6 for the C2 configuration. These instants $t_{i=1,\ldots,6}$ are identified on the sinusoidal evolution of the signal from microphone 5 holding the

https://doi.org/10.1121/10.0008897

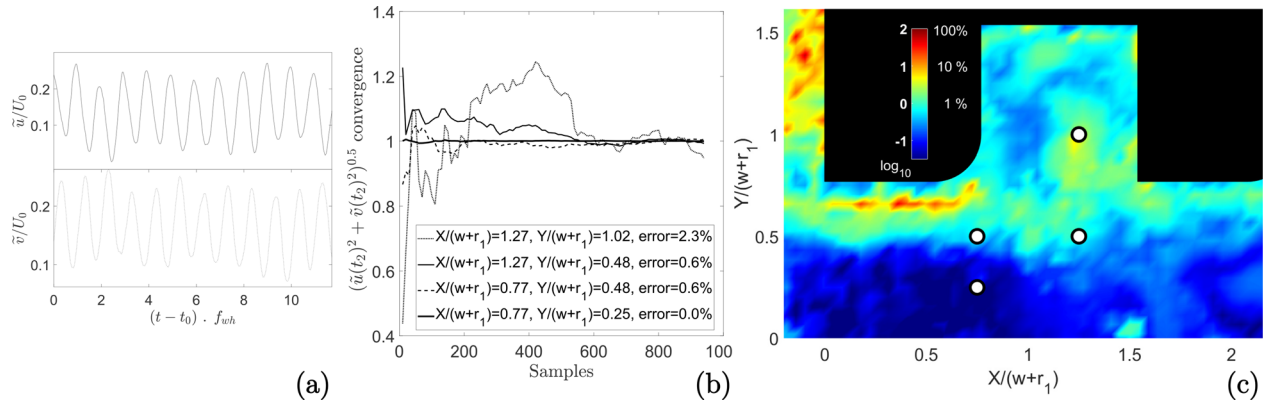

FIG. 12. (Color online) LSE reconstruction for C1 configuration: (a) Non-dimensional $\widetilde{u}$ and $\widetilde{v}$ velocity components reconstructed at high frequency ($Fs = 25\,600$ Hz) by LSE method at the position $[X/(w+r_1) = 1.4, Y/(w+r_1) = 0.8]$ indicated by a white cross-in Fig. 9. (b) Convergence of the magnitude of the instantaneous LSE (non-dimensionalized by the local mean reference value calculated on instantaneous values between 700 to 950 events) for the four positions marked by a black circle on figure (c). (c) Estimation of the standard deviation of fluctuations in the percentage of the local mean reference LSE velocity magnitude calculated in the range 700 to 950 events.

whistling frequency of $f_{wh} = 600$ and 1231 Hz, respectively, with quite the same phase of the microphone signal for the t_i and t_i' instants. The LSE reconstruction not only preserves the characteristics deduced from the analysis of the PIV fields measured at 10 Hz, namely, the presence of a vortex of counterclockwise direction in the first cavity, the vena contracta in the central part of the flow and a recirculation zone trapped between the edge of the vena contracta and the wall, but also quantifies the dynamical interaction between these specific regions of the flow for the C1 configuration. For the C2 configuration, the recirculation zone near the wall, upstream the cavity is not correctly described, because velocity measurements by PIV were precluded due to laser reflection on the wall. Anyway, the hereafter description of the flow synchronisation with the whistling remains actual for both configurations C1 and C2. We observe that the edge of the vena contracta behaves like a flapping jet. Near the top of the rising sinus (t_1), the flow ejected from the cavity is caught by the edge of the vena contracta and the jet moves away from the cavity. Between (t_1) and (t_2), the edge of the vena contracta continues to move away from the cavity and straightens to be aligned parallel to the wall downstream of the cavity. The flow ejected from the cavity vortex then goes upstream by creeping along the rounded edge upstream of the cavity to supply the recirculation zone located between the wall and the vena contracta (t_3). At time (t_4), the recirculation zone continues to be supplied while the jet formed by the edge of the vena contracta impacts the downstream edge of the cavity, that is sharp for C1 and rounded for C2. The lower part of the vortex rolling-up is pushed back outside the cavity. The jet then continues to curve and feeds the vortex in the cavity (t_5). At time (t_6), the jet straightens again and the cycle restarts. These observations confirm exactly, but more clearly the previous observations made by fast camera visualizations at 4000 fps (Mattei *et al.*, 2014) for the C1 configuration. It was also checked that an analysis with phase averaged velocity fields based on synchronization with the signal of Micro 5 gives a similar dynamics with however a less temporal (phase) resolution since the 950 PIV snapshots have to be sorted according to discreet times (phases) giving noisy velocity fields if a high resolution on the discreet times repartition is selected.

In order to isolate the contribution of the flow at the frequency of the dominant mode, an analysis of the temporal signals reconstituted by LSE is carried out at any point of the flow by discrete Fourier transform (DFT). This technique is appropriate here since the signals are well conditioned with a main energy-carrying frequency and a suitable dynamic range avoiding interference between the coefficients from the DFT. The objective is therefore to determine the amplitude and the phase associated with the dominant mode (around 600 Hz here for the C1 configuration) at each

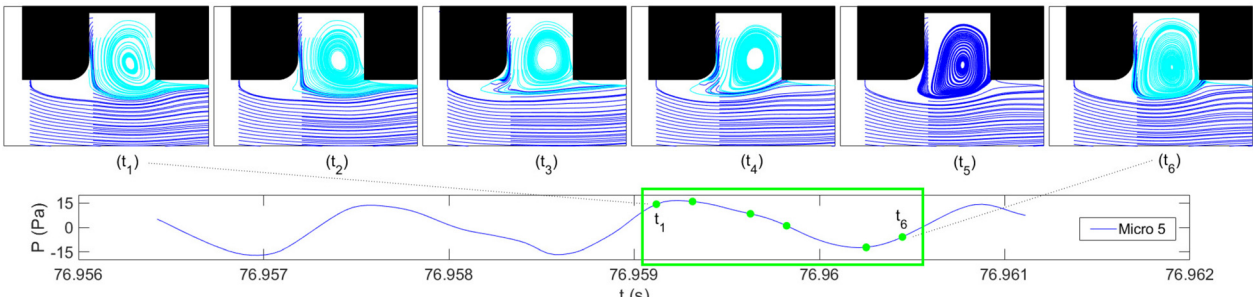

FIG. 13. (Color online) Snapshots of streamlines from LSE at successive phases of the whistling for the configurations C1.

point of the zone reconstituted by LSE. We consider a decomposition of the fluctuating velocity signal reconstituted by the LSE: $\widetilde{U}' = [\widetilde{u}'\ \widetilde{v}']^T$ such as $\widetilde{U}'(x_{pq},t) = \widetilde{U}_{wh}(x_{pq},t) + \widetilde{U'}_0(x_{pq},t)$, where $\widetilde{U}_{wh}(x_{pq},t)$ is the harmonic part at the whistling frequency f_{wh}, $\widetilde{U'}_0(x_{pq},t)$ corresponds to what we call the noisy part, and t is the time sampled at the frequency F_s for a duration T_s. We write

$$\begin{aligned}\widetilde{U}_{wh}(x_{pq},t) &= \widetilde{A}_{wh}(x_{pq}) \times \cos\left(2\pi f_{wh} - \varphi_{wh}(x_{pq})\right) \\ &= \widetilde{Bc}_{wh}(x_{pq}) \times \cos\left(2\pi f_{wh}\right) \\ &\quad + \widetilde{Bs}_{wh}(x_{pq}) \times \sin\left(2\pi f_{wh}\right),\end{aligned} \tag{4}$$

with

$$\begin{cases} \widetilde{A}_{wh}(x_{pq}) = \sqrt{\widetilde{Bc}_{wh}(x_{pq})^2 + \widetilde{Bs}_{wh}(x_{pq})^2} \\ \varphi_{wh}(x_{pq}) = \tan^{-1}\dfrac{\widetilde{Bs}_{wh}(x_{pq})}{\widetilde{Bc}_{wh}(x_{pq})}. \end{cases} \tag{5}$$

The following process consists in identifying the amplitude $\widetilde{A}_{wh}(x_{pq})$ and the phase $\varphi_{wh}(x_{pq})$ for each position (x_{pq}) for both velocity components $Y = [\widetilde{u'}(x_{pq},t)]$ or $Y = [\widetilde{v'}(x_{pq},t)]$. An harmonic decomposition of Y is obtained on a series of K known pulsations $\{\omega_k\}_{k=1,\ldots,K}$ for which the DFT presents peaks larger than a defined threshold. In this series, we identify $\omega_1 = 2\pi f_{wh}$.

Y can then be written as

$$Y = \widetilde{U}_{wh}(x_{pq},t) + \Sigma_{k=2}^{K}\widetilde{Bc}_k C_k + \Sigma_{k=2}^{K}\widetilde{Bs}_k S_k \tag{6}$$

with $C_k = [\cos(\omega_k t)]$ and $S_k = [\sin(\omega_k t)]$ defined for $k = 1,\ldots,K$. The Y vector verifies

$$Y = T\widetilde{B}, \tag{7}$$

where T is a matrix of dimension $T_s F_s \times 2K$ defined by $T = [C_1\, S_1\, C_2\, S_2 \ldots C_k\, S_k]$ with $T_s = 100\,\text{s}$, $F_s = 25\,600\,\text{Hz}$, and $10 \le K \le 14$ for the present analysis, and $\widetilde{B}$ is a matrix of size $2K \times 1$ written as

$$\widetilde{B} = \left[\widetilde{Bc}_1\, \widetilde{Bs}_1, \ldots, \widetilde{Bc}_K\, \widetilde{Bs}_K\right]^T.$$

Pulsations are then defined as $\omega_k = f_k \times 2\pi/F_s$. As $f_k \le F_s/2$, we deduce $\omega_k \in [0,\pi]$; $k = 1,\ldots,K$. This insures the linear independency of the columns of the matrix T. In this case, the matrix T becomes reversible, so that by multiplying Eq. (7) by T^T, $T^T Y = T^T T\widetilde{B}$, we deduce: $\widetilde{B} = (T^T T)^{-1} T^T Y$.

We finally isolate the coefficients $\widetilde{Bc}_{wh}$ and $\widetilde{Bs}_{wh}$ around the whistling frequency f_{wh} in order to calculate the amplitude $\widetilde{A}_{wh}$ given in Fig. 14 and the phase φ_{wh}.

By isolating the part associated with the whistling frequency, what we observe does not correspond to the acoustic field associated with the longitudinal resonance; indeed, the latter should be almost uniform for a given cross section. Our field of view is around $30 \times 20\,\text{mm}^2$ whereas the

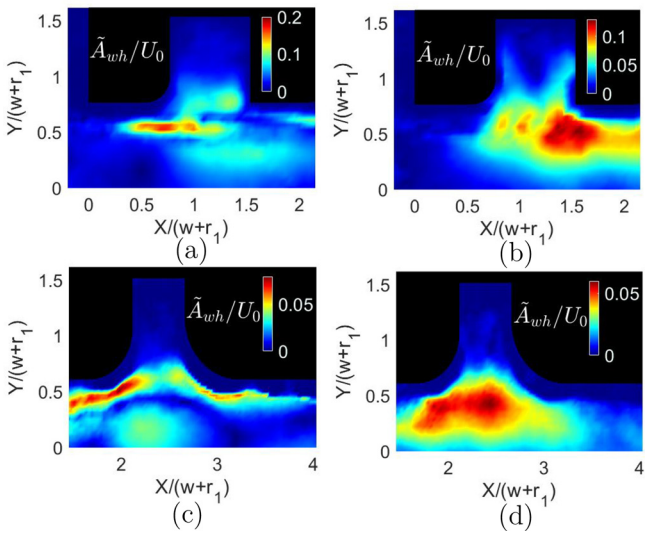

FIG. 14. (Color online) Amplitude $\widetilde{A}_{wh}/U_0$ of the contribution of flow to the velocity fluctuations at the whistling frequency f_{wh} for the $\widetilde{u}_{wh}$ (left side) and $\widetilde{v}_{wh}$ (right side) velocity components. (a) and (b) for the C1 configuration at $f_{wh} = 600\,\text{Hz}$, (c) and (d) for the C2 configuration at $f_{wh} = 1231\,\text{Hz}$.

wavelength associated with the longitudinal mode observed is estimated by $\lambda = C_{eff}/f_{wh} \approx \frac{300}{600} \approx 0.5\,\text{m}$. Thus, we should therefore not be able to observe such a significant variation of the acoustic particle velocity on a field of this dimension. The velocity fluctuations associated with this frequency are therefore representative of an aerodynamic phenomenon imposed by feedback from the acoustics, we should assimilate this contribution as "*pseudo-noise*."

We finally study the case C2. For the latter, the studied cavity is also located at the inlet and therefore at the level of a pressure node. A similar analysis as for the C1 configuration of the LSE reconstructed velocity signal in the observed field is lead with the DFT around the frequency $f_{wh} = 1231\,\text{Hz}$. The maximum amplitude of the acoustic particle velocity is again located at the entrance to the cavity (Fig. 14). The maxima of the amplitudes A_{wh} for $\widetilde{u}_{wh}$ and $\widetilde{v}_{wh}$, respectively, are lower than for the C1 configuration. For both configurations, the turbulence energy is of high level (see Fig. 6) comparatively to the energy level associated with the aero-acoustics contribution. This is in agreement with the spectral analysis of the velocity signal furnished by the hot wire located at the end of the corrugated pipe that has shown that the resonance with a strong amplification occurs only when the energy associated with the resonating mode overcomes the turbulence level.

The representation of the instantaneous velocity field $\widetilde{U}_{wh}(x_{pq},t)$ associated with the whistling at $f_{wh} = 600$ and 1231 Hz for the configurations C1 and C2, respectively, makes it possible to visualize the evolution of vortex structures upon entry. As shown in Fig. 15 emitted vortices progress along the pipe near the region where the instantaneous vorticity component $\omega_z = \partial\widetilde{v}/\partial x - \partial\widetilde{u}/\partial y$ is positive. The irrotational acoustic particle velocity field is not observable since its dynamics is surpassed by that of vortices. In the case of the C1 configuration, one observes, by following the

https://doi.org/10.1121/10.0008897

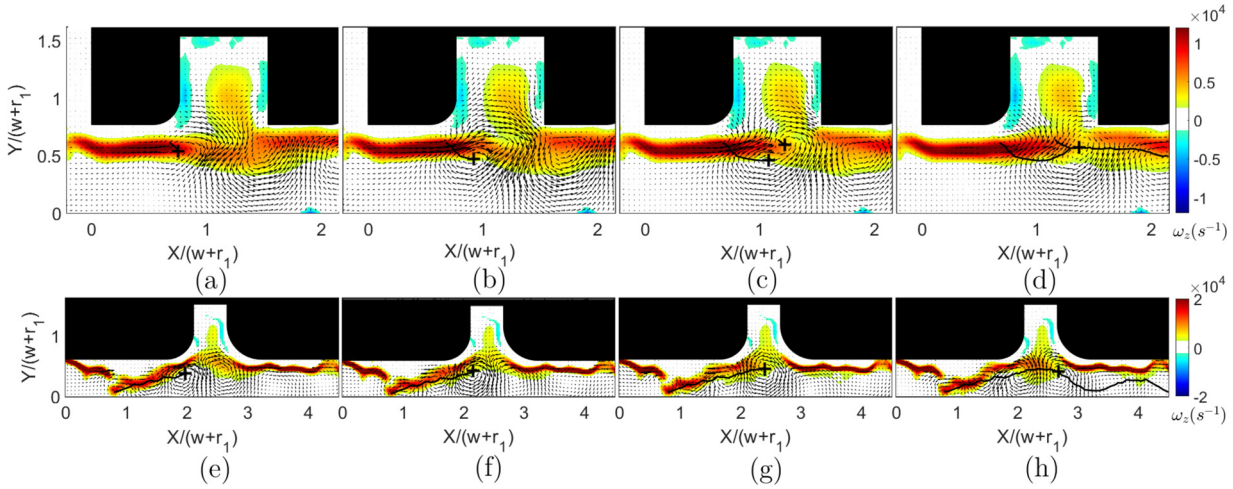

FIG. 15. (Color online) Velocity fluctuations at the whistling frequency: vectors of components $(\widetilde{u}_{wh}, \widetilde{v}_{wh})$. Colored map: instantaneous vorticity ωz (s^{-1}). (a)–(d) Tracking of an emitted vortex at the instants t^2, $t_2 + 6\Delta t$, $t_2 + 12\Delta t$, and $t_2 + 18\Delta t$ for $f_{wh} = 600$ Hz for the C1 configuration. (e)–(h) Tracking of an emitted vortex at the instants t'_2, $t'_2 + 4\Delta t$, $t'_2 + 8\Delta t$, and $t'_2 + 12\Delta t$ for $f_{wh} = 1231$ Hz for the C2 configuration, with $\Delta t = 1/25\,600$ s. The instant t_2 (and t'_2 too, respectively) corresponds to a maximum of Micro5 signal as in Fig. 13. (–) Vortex trajectory, (+) Clockwise vortex center.

movement of a clockwise vortex [Fig. 15(a)–15(d)], that it originates at the boundary of the instantaneous vorticity zone directly above the upstream rounded edge of the cavity when the acoustic particle velocity at X = 0, identified to the upstream velocity HW2 signal, centered and filtered at f_{wh}, is maximum. The clockwise vortex then moves away from the cavity opening, while a second clockwise vortex originates in the flapping region of the vorticity band plumb with the center of the cavity opening when the acoustic particle velocity signal crosses zero in the descending phase. The two vortices pair up just before to be plumb with the sharp downstream edge of the first cavity when the acoustic particle velocity reaches its minimum value, then the resulting vortex runs in the main flow along the plateau that exists just after the first cavity. The next step is that the vortex reaches the upstream rounded edge of the second cavity after a period of whistling, having thus traveled the length of one pitch. Over this length of one pitch, at every moment, one observes a pair of counter-rotating vortices. In the case of the C2 configuration [Fig. 15(e)–15(h)], a clockwise vortex also originates at the boundary of the vorticity zone, but rather on the plateau which precedes the first cavity and not just directly above the upstream rounded edge; this position of the vortex is synchronized with a zero crossing of the acoustic particle velocity. The vortex is then plumb with the upstream edge of the cavity after having traveled a distance $(w + r_1)$ during a period of the whistle, the acoustic particle velocity therefore falling again to zero and Micro5 signal rising a maximum at the instant t'_2 [Fig. 15(e)]. Along this path, the size of the vortex increases, reaching a maximum diameter, around (w + r1), directly above the cavity [Fig. 15(g)] when the acoustic particle velocity is at its maximum. After the cavity opening, vortices continue by skirting the downstream edge, towards the main flow, as similarly observed for vortex path downstream a side-branch opening in the vortex induced-pulsation in gas system studied by Kriesels *et al.* (1995). Over a longitudinal distance of one pitch, two pairs of counter-rotating vortices are observed. This mechanism is rather different of the sound production associated with the Rossiter modes of a single shallow cavity where the shear layer hits the downstream edge of the cavity. Nevertheless, if we estimate the frequency $f_{c,m}$ associated with the Rossiter mode m of the cavity with the equation of Rossiter (1964), one calculates $f_{c,m} = (U_0/l)\,[(m - \alpha)/(1/k + M)]$ with l the width at the cavity aperture, so we consider $l = L + r_1$ for C1 and $l = L + r_1 + r_2$. According to Rossiter study, α is 0.25 for a deep cavity with $l/H \approx 1$. k is equal to the ratio U_c/U_0, we consider $k = 0.5$ as shown hereafter from the analysis of convected vortices. For the configuration C1, the frequency associated with the first Rossiter mode ($m = 1$) of the cavity is estimated at $f_{c,m=1} = 604$ Hz for $M = 0.063$, while $f_{c,m=1} = 884$ Hz for C2 for $M = 0.069$. Whereas there is no agreement between pipe mode and Rossiter cavity mode frequencies for the C2 configuration, it is interesting to note the proximity of these frequencies for the C1 configuration, this may contribute to explain the higher level of $U_{rms}\rho_0 c_0$ of the main modes for C1 than for C2 for similar Mach numbers [Fig. 8(d)].

As a reminder, at each point in the field, the velocity that we observe here is a sinusoid of frequency corresponding to the frequency of the whistle f_{wh}. We thus observe vortices characteristic of the whistle propagating at the velocity of the flow in the zone. This phenomenon is repeated over time and independent of the initial time. In the presence of the strong whistling, the vortices are organized around the excited resonant frequency. These propagate at the velocity of the flow, namely, at the convection velocity U_c near the wall. Along a one-pitch long path of the clockwise vortices identified in Fig. 15, ones estimates $U_c \approx 11.0\,\mathrm{m\,s^{-1}} = 0.51\mathrm{U}_0$ and $U_c \approx 11.8\,\mathrm{m\,s^{-1}} = 0.50\mathrm{U}_0$, respectively, for the configurations C1 and C2, that are in the expected range for the convection velocity. This may be assimilated to *pseudo-noise* associated with coherent structures the fluctuation levels of which greatly exceed the fluctuation levels

associated with the acoustic resonance frequency. As also observed in industrial riser (Mattei *et al.*, 2018), during whistling the velocity signal propagates along the pipe at the convective flow velocity while its frequency corresponds here to a longitudinal acoustics resonance. Acoustic feedback on the flow is thus highlighted.

D. Acoustic power estimation

An estimation of acoustic power associated with this vortex shedding is performed using the approach initiated by Powell (1964) and extended by Howe (1975) (Howe, 2002). In this model, the instantaneous acoustic power P_w generated by the vorticity of the flow, $\vec{\omega} = \nabla \times \vec{u}$, within a volume v, can be obtained from $P_w(x,y,t) = -\rho_0 \int\int\int_v \vec{u}_{ac} \cdot(\vec{\omega} \times \vec{u})\, dv$, where ρ_0 is the fluid density, u is the fluid velocity, and u_{ac} is the acoustic particle velocity. The instantaneous LSE reconstituted velocity field $\vec{u} = \tilde{\vec{u}}$ is used here in the flow contribution to the acoustic power integral.

Since the acoustic particle velocity $\vec{u}_{ac}$ is not directly measured in the whole field of view in the present experiments, it is assimilated to the V-velocity field of a potential, irrotational flow whose amplitude is given by the velocity measured at the corrugated pipe entry. One identifies $u_{ac}(x=0,y,t) = u'_{wh}(t)$, where $u'_{wh}(t)$ is the velocity signal measured by the upstream hot wire probe HW2, centered and filtered at f_{wh}. The velocity potential ψ from which the velocity V is derived ($\vec{V} = \vec{\nabla}\psi$) satisfies the Laplace equation $\Delta\psi = 0$. The equation is solved in FREEFEM++ environment. The 2D domain of calculation around the first cavity is delimited by $0 < X < 2Pt - (r_1 + w + r_2)$ and $-(D/2 + H) < Y < (D/2 + H)$. A finite triangular element mesh with an adaptative mesh refinement is performed, resulting in 3400 and 1700 elements for the C1 and C2 configurations, respectively. The boundary conditions are Neumann conditions: $\partial\psi/\partial n = -u'_{wh}(t)$ at X=0, $\partial\psi/\partial n = u'_{wh}(t)$ at $X = 2Pt - (r1 + w + r2)$, and $\partial\psi/\partial n = 0$ on walls, with $\vec{n}$ the local outer normal vector. The velocity field $V(x,y,t)$ calculated at each time step is corrected by its spatial dependance on the considered mode so that $u_{ac}(x,y,t) = V(x,y,t) \cdot\cos(2\pi F_{wh} X/c_{eff})$. Even if this analytical form of $u_{ac}(x,y,t)$ does not respect strictly $\nabla \times \vec{u}_{ac} = 0$, it was verified that the space-time averaged values of $\nabla \times \vec{V}$ and $\nabla \times \vec{u}_{ac}$ are 0.0022 and 0.0021 s^{-1}, respectively; the irrotationality is thus similarly respected for both fields u_{ac} and V.

Figure 16 illustrates the results of this simulation for the two configurations C1 and C2. Figure 16(a) presents the axial profile of the transversal component u_{ac_y} of the acoustic velocity near the cavity opening, at $Y = 95\%D/2$. For the configuration C1, the profile is clearly asymmetrical on either side of the X_{c_1} abscissa because of the downstream sharp edge ($r_2 = 0$). The streamlines of the acoustic velocity fields are drawn for both the configurations on Figs. 16(b) and 16(c).

Figures 17(a) and 17(b) highlight the spatial contribution to the instantaneous acoustic power $P_w(x,y,t)$ of two regions in the vicinity of the first cavity for the configuration C1. One is located at the edge of the vena contracta and the recirculation zone located on the plateau at the entrance and the other on the sharp downstream corner of the corrugation. These two regions contribute alternately as a source [$P_w(x,y,t) > 0$] or a sink [$P_w(x,y,t) < 0$] when the signal $u'_{wh}(t)$ reaches an extreme value, positive or negative, respectively. For the C2 configuration [Figs. 17(e), 17(f)], four patterns of alternative signs contribute to $P_w(x,y,t)$. The temporal integration ($\langle . \rangle$) on these patterns specifies the spatial distribution of $\langle P_w(x,y)\rangle$; the result is similar for the two configurations, namely, a positive contribution from the regions located on the edges of the cavity, while the opening of the cavity would rather be a sink [Figs. 17(c), 17(g)].

The chosen integration volume $V_{one-pitch}$ is that of a portion of corrugated tube with a length of one pitch and span B in the vicinity of the first cavity. We choose X varying from 5 to 25 mm for C1 and 0 to 20 mm for C2, so as to cover the region of significant contribution to $P_w(x,y,t)$. Y varies from 0 to $D/2 + H$, while, under the black patches of solid wall, the value to be integrated is zero. The temporal evolution of $P_w(t)$ [Figs. 17(d), 17(h)] is deduced from the spatial integration of $P_w(x,y,t)$ over the integration volume defined above. For the C1 configuration, $P_w(t)$ is mostly positive and the space-time average acoustic power is estimated at $\langle P_w \rangle = 4.05 \times 10^{-3}$ W which corresponds to 96.1 dB for a value of reference taken at 10^{-12} W. This value is to be compared with the estimate of the average acoustic power $\langle P_{w_{pipe\ end}} \rangle$ radiated at the downstream end of the corrugated pipe.

Considering that at the downstream end of the pipe, the acoustic waves are radiated and convected by the average flow, we express the instantaneous acoustic power

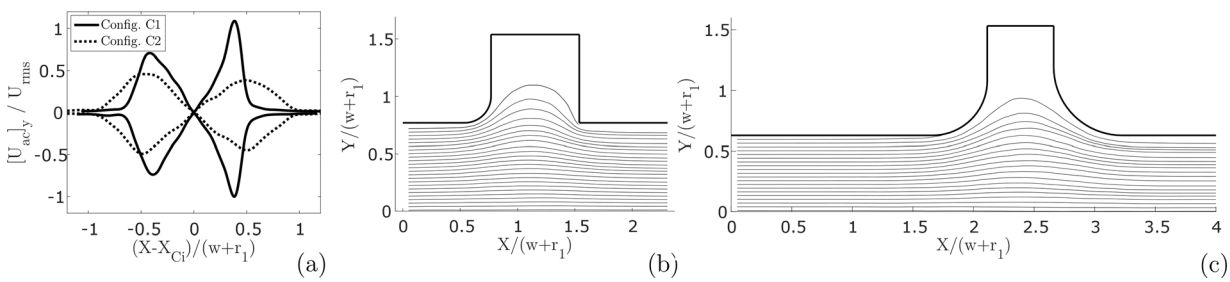

FIG. 16. Simulations of irrotational potential flows. (a) Axial profile on the cavity opening length (at $Y = 95\%D/2$) of the calculated transversal acoustic particle velocity amplitude non-dimensionalized by the velocity root mean square of the main mode at the pipe entry, for each configuration C1 and C2, respectively (axial offsets $X_{C_{i=1,2}}$: $X_{C_1}/(w + r_1) = 1.1$ and $X_{C_2}/(w + r_1) = 2.4$). (b), (c) Streamlines for C1 and C2 configurations.

https://doi.org/10.1121/10.0008897

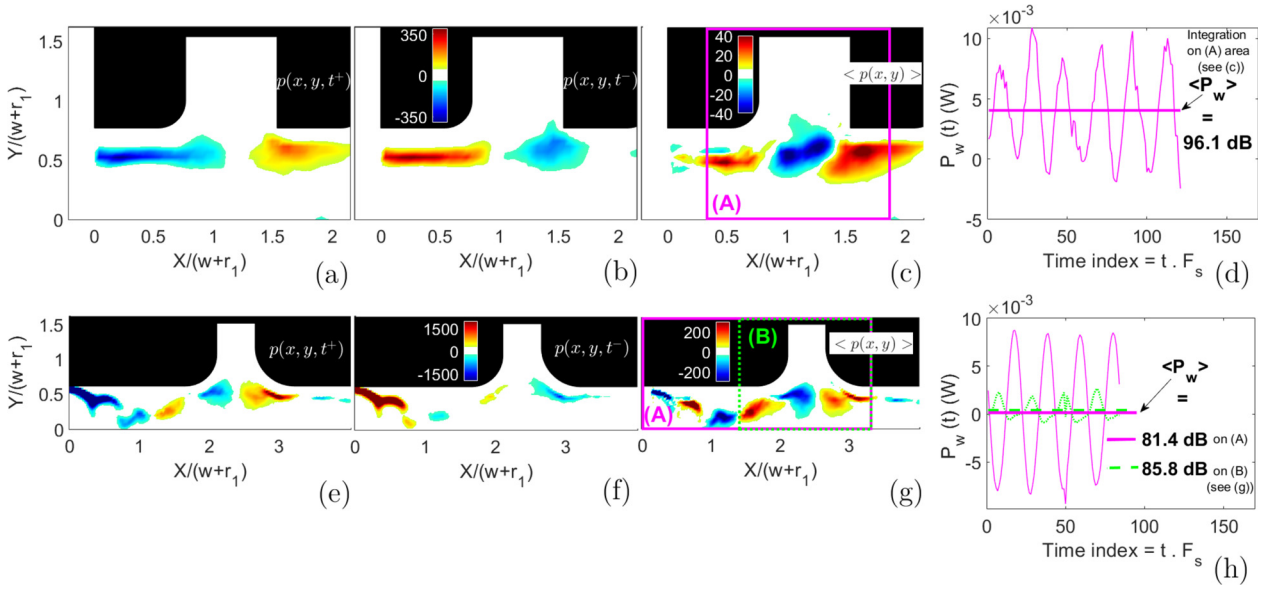

FIG. 17. (Color online) Estimations of acoustic power with Howe model, up for C1, down for C2. (a), (b) Instantaneous normalized acoustic power density $p(x,y,t) = P_w(x,y,t)/(P_{w_{pipe-end}}/V_{one-pitch})$ patterns for two instants t+ and t– corresponding to maximal and minimal values of u'_{HW2}, respectively. (c) Time-averaged patterns of normalized acoustic power $\langle p(x,y)\rangle = \langle P_w(x,y)\rangle/(P_{w_{pipe-end}}/V_{one-pitch})$. (d) Instantaneous one pitch-volume integrated acoustic power $P_w(t)$, decibel reference: 10^{-12} W. (e)–(h) Idem for C2 configuration. The averaged acoustic power $\langle P_w\rangle$ values given in (d) and (h) are calculated over the solid (A) and dotted (B) rectangles plotted in (c) and (g).

$P_{w_{pipe-end}} = S_{out} \cdot p_{ac}(\omega) \cdot u_{ac}(\omega)$, where S_{out} is the exit section of the pipe end and p_{ac} the acoustic pressure. Following the approach of Rudenko *et al.* (2013) for a round corrugated pipe, the pipe end impedance that links p_{ac} and u_{ac} is written as $Z_{out} = \rho_0 c_0 (\omega D_{out}/4c_0)^2 + \rho_0 c_0 M$, where $c_0 = 343\,\mathrm{m\,s^{-1}}$ is the speed of sound, $\omega = 2\pi f_{wh}$ is the pulsation, and D_{out} is the exit diameter of the round pipe end. By analogy, the diameter D_{out} is identified as the hydraulic diameter for the present rectangular cross section pipes C1 and C2, so that $D_{out} = (4 \times Cross\,section)/Perimeter = 2DB/(D+B)$ and so $S_{out} = (\pi D_{out}^2)/4$. The acoustic power is then expressed as $P_{w_{pipe-end}} = Z_{out} \cdot S_{out} \cdot u_{ac_{rms}}^2$, where $u_{ac_{rms}}$ is the acoustic velocity root mean square at the pipe end identified as the root mean square of the hot wire velocity signal filtered at the whistling frequency of the main mode for the considered Mach number M [see Fig. 8(d)]. With $u_{ac_{rms}} = 0.278\,\mathrm{m\,s^{-1}}$ for the configuration C1, one calculates $\langle P_{w_{pipe\,end}}\rangle = 1.98 \times 10^{-3}$ W corresponding to 93.0 dB that is quite comparable with the value of averaged acoustic power associated with the vortex shedding around the first corrugation with the Howe model. For the C2 configuration, we highlight the contribution of six patterns of alternative signs on the representation of $\langle P_w(x,y)\rangle$ [Fig. 17(g)] whose characteristic length is as for the C1 configuration [Figure 17(c)] close to the width w of the considered cavity. Figure 17(h) shows that the spatial integration $P_w(t)$ oscillates around zero, the time averaging over several periods, nevertheless positive: $\langle P_w\rangle = 1.38 \times 10^{-4}$ W (81.4 dB) is, however, not significant because the velocity measurements very close to the wall of the input plateau are not sufficiently resolved to conclude on the sound power level over the observed zone corresponding to one pitch. When selecting the region that includes the cavity and, the upstream and downstream rounded edges [dotted rectangular area in Fig. 17(g)], the contributions of the only three larger patterns near the cavity opening, similarly to the C1 configuration, give an instantaneous sound power with lower amplitude oscillations but with a clearer net positive balance estimated to 85.8 dB. Note that the average sound power radiated at the downstream end of the corrugated pipe is estimated at $P_{w_{pipe-end}} = 2.52 \times 10^{-5}$ W corresponding to 74.0 dB with $u_{ac_{rms}} = 0.0701\,\mathrm{m\,s^{-1}}$, that is globally in a good agreement with lower acoustic levels observed for C2 compared to C1 [Figs. 8(c), 8(d)].

VII. CONCLUSION

The flow in the vicinity of the first cavity has been investigated for two configurations of corrugated pipes in order to understand the feedback between the acoustics and the structuration of the flow. The reconstruction of the instantaneous velocity fields by linear stochastic estimation based on PIV and probes measurements has given quantitative information on the flow organization with spatial and temporal resolutions not reachable with usual optical diagnostics. For both geometries of the studied corrugated pipes, the region of the flow that contributes to acoustic level is confirmed to be located in the shear layer. A flapping of the vena contracta near the pipe entry is combined with an oscillation of the vortex inside the cavity and with vortex shedding emitted in the wake of the rounded upstream edge of the cavity. For the narrow cavity that is also associated with a narrow gap between face to face corrugated walls for the second configuration, these vortices are better structured and smaller than for the first configuration. While these vortices travel along the cavity aperture at a convection velocity of $0.5\,U_0$ as expected in a shear layer near a wall, they carry a

velocity signal synchronized with the whistling frequency of the resonating longitudinal mode. The energy level of the fluctuating velocity at whistling frequency is high and is related to *pseudo-noise* or "*vortex noise*."

VIII. ACKNOWLEDGMENTS

This work was funded by TOTAL E&P RECHERCHE DEVELOPPEMENT. The support of J. P. Roques and his collaborators all along this research is gratefully acknowledged. The authors also thank the reviewers and D. Mazzoni for their helpful comments.

Adrian, R. J. (**1979**). "Conditional eddies in isotropic turbulence," Phys. Fluids **22**(11), 2065–2070.

Adrian, R. J., and Moin, P. (**1988**). "Stochastic estimation of organized turbulent structure: Homogeneous shear flow," J. Fluid Mech. **190**, 531–559.

Amielh, M., Jiang, Y., Anselmet, F., Kristiansen, U., Mattei, P.-O., Mazzoni, D., and Pinhède, C. (**2014**). "Aeroacoustic source analysis in a corrugated flow pipe using low-frequency mitigation," J. Turbul. **15**(10), 650–676.

Durgesh, V., and Naughton, J. W. (**2010**). "Multi-time-delay LSE-POD complementary approach applied to unsteady high-Reynolds-number near wake flow," Exp. Fluids **49**, 571–583.

Geveci, M., Oshkai, P., Rockwell, D., Lin, J.-C., and Pollack, M. (**2003**). "Imaging of the self-excited oscillation of flow past a cavity during generation of a flow tone," J. Fluids Struct. **18**, 665–694.

Golliard, J., and Tonon, D. (**2010**). "Whistling of short corrugated pipes: Experimental investigation of the source location," in *Proceedings of the 6th AIAA/CEAS Aeroacoustics Conference*, Lahaina, HI.

Graziani, A., Fadla, F., Lippert, M., Kerhervé, F., Mathis, R., Uystepruyst, D., and Keirsbulck, L. (**2015**). "Estimation stochastique d'un écoulement décollé en aval d'une bosse par méthode électrochimique," in *22ème Congrès Français de Mécanique*, Lyon, France.

Hammache, M., Rohr, J., and Gharib, M. (**1993**). "Active control of flow induced resonance in continuous corrugated tubes," Technical Report No. AD-A 265782.

Howe, M. (**2002**). *Cambridge Texts in Applied Mathematics Theory of Vortex Sound* (Cambridge University Press, Cambridge).

Howe, M. S. (**1975**). "Contributions to the theory of aerodynamic sound, with application to excess jet noise and the theory of the flute," J. Acoust. Soc. Am. **71**, 625–673.

Koschatzky, V., Moore, P. D., Westerweel, J., Scarano, F., and Boersma, B. J. (**2011a**). "High speed PIV applied to aerodynamic noise investigation," Exp. Fluids **50**, 863–876.

Koschatzky, V., Westerweel, J., and Boersma, B. J. (**2011b**). "A study on the application of two different acoustic analogies to experimental PIV data," Phys. Fluids **23**, 065112–065112–15.

Kriesels, P. C., Peters, M. C. A. M., Hirschberg, A., Wijnands, A. P. J., Iafrati, A., Riccardi, G., Piva, R., and Bruggeman, J. C. (**1995**). "High amplitude vortex-induced pulsations in a gas transport system," J. Sound Vib. **184**(2), 343–368.

Mahmoodi-Jezeh, S. V., and Wang, B.-C. (**2020**). "Direct numerical simulation of turbulent flow through a ribbed square duct," J. Fluid Mech. **900**, A18-1–A18-43.

Mattei, P.-O., Amielh, M., Roques, J.-P., Karnikian, A., Galeron, G., Décuupère, M., and Charliac, D. (**2018**). "Experimental analysis of the whistling of an industrial riser," in *The Second International Conference on Acoustics and Vibration, ICAV–2018*, Hammamet, Tunisia.

Mattei, P.-O., Mazzoni, D., Amielh, M., Jiang, Y., and Kristiansen, U. (**2014**). "Contrôle des résonances acoustiques d'un tuyau corrugué sous écoulement," in *12ème Congrès Français d'Acoustique, CFA 2014*, Poitiers, France.

Nakamura, Y., and Fukamachi, N. (**1984**). "Sound generation in magic pipes," J. Jpn. Soc. Fluid Mech. **3**, 199–203.

Nakamura, Y., and Fukamachi, N. (**1991**). "Sound generation in corrugated tubes," Fluid Dyn. Res. **7**, 255–261.

Nakiboglu, G. (**2012**). "Aeroacoustics of corrugated pipes," Ph.D. dissertation, Department of Applied Physics, Eindhoven University of Technology, the Netherlands.

Nakiboglu, G., Belfroid, S. P. C., Golliard, J., and Hirschberg, A. (**2011**). "On the whistling of corrugated pipes: Effect of pipe length and flow profile," J. Fluid Mech. **672**, 78–108.

Nakiboglu, G., Belfroid, S. P. C., Willems, J. F. H., and Hirschberg, A. (**2010**). "Whistling behavior of periodic systems: Corrugated pipes and multiple side branch system," Int. J. Mech. Sci. **52**, 1458–1470.

Nakiboglu, G., and Hirschberg, A. (**2012**). "Aeroacoustic power generated by multiple compact axisymmetric cavities: Effect of hydrodynamic interference on the sound production," Phys. Fluids **24**, 067101–067101–18.

Pey, Y. Y., Chua, L. P., and Siauw, W. L. (**2012**). "Stochastic estimation of cavity flowfield," World Acad. Sci. Eng. Technol. **6**, 11–26.

Piponniau, S., Collin, E., Dupont, P., and Debiève, J. F. (**2014**). "Estimation stochastique linéaire d'une interaction onde de choc-couche limite turbulente," in *14ème Congrès Francophone de Techniques Laser (CFTL2014)*, Marseille, France.

Popescu, M., Johansen, S. T., and Shyy, W. (**2011**). "Flow-induced acoustics in corrugated pipes," Commun. Comput. Phys. **10**, 120–139.

Powell, A. (**1964**). "A theory of vortex sound," J. Acoust. Soc. Am. **36**, 177–195.

Rossiter, J. E. (**1964**). "Wind-tunnel experiments on the flow over rectangular cavities at subsonic and transonic speeds," Aeronautical Research Council Reports and Memoranda, Technical Report No. 3438.

Rudenko, O., Nakiboğlu, G., Holten, A., and Hirschberg, A. (**2013**). "On whistling of pipes with a corrugated segment: Experiment and theory," J. Sound Vib. **332**, 7226–7242.

Tinney, C. E., Coiffet, F., Delville, J., Hall, A. M., Jordan, P., and Glauser, M. N. (**2006**). "On spectral linear stochastic estimation," Exp. Fluids **41**(5), 763–775.

Tonon, D., Landry, B. J. T., Belfroid, S. P. C., Willems, J. F. H., Hofmans, G. C. J., and Hirschberg, A. (**2010**). "Whistling of a pipe system with multiple side branches: Comparison with corrugated pipes," J. Sound Vib. **329**, 1007–1024.

Vinuesa, R., Noorani, A., Lozano-Duran, A., El Khoury, G. K., Schlatter, P., Fischer, P. F., and Nagib, H. M. (**2014**). "Aspect ratio effects in turbulent duct flows studied through direct numerical simulation," J. Turbul. **15**(10), 677–706.

Vinuesa, R., Schlatter, P., and Nagib, H. M. (**2018**). "Secondary flow in turbulent ducts with increasing aspect ratio," Phys. Rev. Fluids **3**, 054606.

Zhang, Y., Cattafesta, L. N., and Ukeiley, L. (**2020**). "Spectral analysis modal methods (SAMMS) using non-time-resolved PIV," Exp. Fluids **61**, 226–239.